RSC Advances

ROYAL SOCIETY OF CHEMISTRY

www.rsc.org/advances

Journal Name

ARTICLE

Dispersed SnO_2 nanoparticles on MoS_2 nanosheets for superior gas-sensing performances to ethanol

Received 00th January 20xx,
Accepted 00th January 20xx

DOI: 10.1039/x0xx00000x

www.rsc.org/

Huihui Yan, Peng Song,* Su Zhang, Zhongxi Yang and Qi Wang

The unique properties of MoS_2 nanosheets make them promising supporting substrate for preventing the interparticle aggregation of metal-oxide-semiconductor nanomaterials. A novel composites were successfully obtained by a two-step low temperature hydrothermal method for the synthesis of SnO_2 nanoparticles dispersing on the surfaces of MoS_2 nanosheets. The morphology and structure of the as-prepared samples were characterized by X-ray diffraction (XRD), X-ray photoelectron spectra (XPS), field emission scanning electron microscopy (FESEM), and transmission electron microscopy (TEM). Owing to the supporting substrate of specific two-dimensional MoS_2 nanosheets and the superior gas-sensing performance offered by ultrasmall SnO_2 nanoparticles, the sensor based on SnO_2@MoS_2 composites exhibit high response and good selectivity to ethanol gas.

Introduction

Metal-oxide-semiconductor (MOS) nanomaterials with small sizes exhibit high sensitivity for gas detection, owing to the fact that chemical interaction of gas molecules with the semiconductor's surface leads to changes in the electrical conductivity.[1-3] The n-type metal oxide semiconductor gas sensors, such as SnO_2, ZnO, and Fe_2O_3 have been employed in commercial applications.[4-6] Of all the sensing materials currently investigated, tin dioxide (SnO_2) nanomaterials have attracted considerable attention, because of their wide applications in lithium-ion batteries, gas sensors, sensitized solar cells, and catalysts.[7] To improve the gas sensing performance, many novel SnO_2 nanostructures, such as zero-dimensional (0D) nanoparticles,[8] one-dimensional (1D) nanowires,[9] two-dimensional (2D) nanosheets,[10] and three-dimensional (3D) hierarchical architectures,[11] have been reported. However, the strong interactions of metal oxides nanomaterials, especially for their nanostructured counterparts, cause them to clump and aggregate, thereby deteriorating the sensing performance. Accordingly, dispersing metal oxide nanostructures on various supporting substrates is regarded as a very promising approach for preventing the interparticle aggregation.[12-16]

Among various substrates, two-dimensional (2D) supporters are appealing candidates because they provide a platform for attaching the nanostructures. Graphene, composed of monolayers of carbon atoms arranged in a honeycombed network, is a robust substrate due to its advantages of atomically smooth surfaces, transparency, nontoxicity, and structural stability.[17] So far, graphene is a good supporting substrate for dispersing metal oxide nanostructures. For instance, Neri et al. investigated the sensing behavior of SnO_2/reduced graphene oxide nanocomposites toward NO_2.[18] Liang et al. have shown that the synthesized α-Fe_2O_3@graphene nanocomposites behave enhanced gas-sensing property to ethanol.[19] However, the lack of a band gap in graphene significantly limits its application.[20] In addition to graphene, MoS_2 has been attracting increasing attention because of its significant direct band gap (1.8 eV), large surface-to-volume ratio, and outstanding field-effect transistor (FET) behavior. Layered MoS_2 is one of the typical graphene analogues. Owing to the specific 2D confinement of electron motion and the absence of interlayer perturbation, the MoS_2 monolayer possesses a direct band gap.[21-23] The unique properties of MoS_2 nanosheets make them a promising candidate for high-performance sensing materials.[24-26] Surprisingly, as compared to the significant progress achieved in the graphene-based gas-sensing materials, the MoS_2-supported composites have been lingering far behind. As far as we know, few studies on the gas-sensing properties of metal oxide/MoS_2 composites have been reported. As compared to the significant progress achieved in the graphene-based gas-sensing materials, the MoS_2-supported composites have been lingering far behind.

Herein, we develop a two-step low temperature hydrothermal method for the synthesis of SnO_2 nanoparticles dispersing on the surfaces of MoS_2 nanosheets. To synthesize MoS_2 nanosheets, sodium molybdate was chosen as the precursor for molybdenum and thioacetamide was used as the sulfur source. During the subsequent hydrothermal treatment, MoO_4^{2-} anions

School of Material Science and Engineering, Shandong Provincial Key Laboratory of Preparation and Measurement of Building Materials, University of Jinan, Jinan 250022, China. E-mail: mse_songp@ujn.edu.cn

Electronic Supplementary Information (ESI) available: [XPS spectra, FESEM and TEM images of MoS_2 nanosheets, and FESEM images and gas response of SnO_2@MoS_2 composites at different molar ratio]. See DOI: 10.1039/x0xx00000x

were reduced under high temperature condition, forming MoS_2 nanosheets without adding any 2D substrate. SnO_2 nanoparticles were prepared using a simple hydrothermal method and dispersed onto MoS_2 nanosheets. A comparative study between pure SnO_2 nanoparticles and SnO_2@MoS_2 composites was performed to reveal the promotion effect of MoS_2 nanosheets on gas-sensing performance. Experimental results showed that SnO_2@MoS_2 composites exhibit superior gas-sensing performance to ethanol in comparison with pure SnO_2 nanoparticles. A possible sensing mechanism was also proposed for the SnO_2@MoS_2 composites.

Experimental

Synthesis of MoS_2 nanosheets

All the chemical reagents were analytical graded and used without further purification. The MoS_2 precursors were synthesized through a simple hydrothermal method. In a typical reaction, 2 mmol of sodium molybdate ($Na_2MoO_4 \cdot 2H_2O$) and 9 mmol of thiocarbamide (CH_4N_2S) were mixed and dissolved in 70 ml deionized water. After stirring the solution for 30 min, 2.2 mmol of citric acid ($C_6H_8O_7 \cdot H_2O$) was added into the above solution. After magnetically stirring for 10 min, the homogeneous solution was transferred into a 100 ml Teflon-lined stainless steel autoclave, sealed tightly, and maintained at 200 ^oC for 21 h. After the hydrothermal procedure, the autoclave cooled down to room temperature spontaneously. The black precipitates were collected by centrifugation, washed several times with deionized water and absolute ethanol, respectively, and dried at 60 ^oC for 12 h in air.

Synthesis of SnO2@MoS2 composites

The synthesis of SnO_2@MoS_2 composites were used by the hydrothermal method. The as-fabricated MoS_2 (0.1 g) was dissolved in 80 ml deionized water and ultrasonic dispersion 20 min to ensure the black powders was completely dispersed in the solution. $SnCl_2 \cdot 5H_2O$ (0.438 g) and NaOH (0.3 g) dissolved in the solution. After magnetic stirring for 30 min, a suspension was obtained and transferred into a 100 ml stainless steel autoclave with Teflon-lined, which was heated at 180 ^oC for 18 h. After the autoclave was cooled down to room temperature, the precipitates were collected and washed several times with deionized water and ethanol, respectively. After drying at 60 ^oC for 6 h, the ashen powders were obtained.

Characterization

The crystal structure and phase composition of as-prepared samples were identified by X-ray diffraction (XRD, Bruker D8 Advance) using Cu*Ka*1 radiation (λ = 0.15406 nm) at 30 kV and 40 mA at a scanning rate of 2° at 2θ min^{-1}. The morphology and nanostructure of the products were characterized using FEI Sirion 200 field emission gun scanning electron microscope (FESEM, Hitachi S4800), and transmission electron microscopy (TEM, Hitachi H-800). More details about the structure were investigated by the selected area electron diffraction (SEAD) pattern and high resolution transmission electron microscopy (HRTEM, JEOL 2010). X-ray photoelectron spectra (XPS) were measured using a PHI 5300 X-ray photoelectron spectrometer with Al K*a* radiation.

Fabrication and measurement of gas sensor

The obtained samples were firstly mixed with distilled water to form slurry through milling, and then pasted onto a prefabricated alumina tube (7 mm in length and 1.5 mm in diameter, attached with a pair of gold electrodes and platinum wires) by a small brush to form a thick film. The thickness of sensing films was about 100 μm. A Ni-Cr resistor (diameter = 0.5 mm, resistance = 35 Ω) in the inner alumina ceramic tube, as a heater, was used to provide the working temperature for the sensor device. After dried in the air and aged at 300 ^oC for 2 days, it has been an indirectly-heated gas sensor, and then the gas sensor was putted into the test chamber in a measuring system of WS-30A (Winsen Electronics Co. Ltd., Zhengzhou, China) by a static process. A typical testing procedure was as follows: The sensors were put into a glass chamber (18 L) at the beginning. When the resistances of all the sensors were stable, the calculated amount of the target gas or liquid was injected into glass chamber by a micro-injector and mixed with air. For the target gases obtained from liquid, the concentration of target gas was calculated by the following formula,

$$C = (22.4*\rho*d*V_1)/(M*V_2) \quad (1)$$

where C (ppm) is the target gas concentration, ρ (g/mL) is the density of the liquid, d is the purity of the liquid, V_1 (μL) is the volume of the liquid, V_2 (L) is the volume of the glass chamber, and M (g/mol) is the molecular weight of the liquid. The working temperature of the sensor can be controlled by adjusting the heating voltage ($V_{heating}$) across a Ni-Cr alloy resistor inside the ceramic tube. A reference resistor (R_{load}) is put in series with the sensor to form a complete measurement circuit. In the test process, a working voltage of 5 V ($V_{working}$) was applied. By monitoring the voltage across the reference resistor (V_{output}), the response of the sensor in air or in a test gas could be measured. The sensor response was defined as,

$$Response = R_{gas}/R_{air} \quad (2)$$

where R_{air} is the resistance of the sensor in air and R_{gas} is the resistance of sensor in the presence of the test gas.

Results and discussion

The purity and crystalline phase of as-synthesized pure MoS_2, SnO_2 nanoparticles and SnO_2@MoS_2composites were analyzed by a powder X-ray diffractogram. Fig. 1 shows the XRD patterns of the samples, which displays diffraction peaks in the range of 10-80°. As for the pure MoS_2 sample, the detected peaks at 2θ = 14.4^o, 33.1^o, 39.7^o and 58.5^o can be assigned to the (002), (100), (103) and (110) planes in the hexagonal phase of MoS_2 (JCPDS 37-1492). Moreover, the diffraction peaks of SnO_2 can be easily indexed to a pure tetragonal rutile structured tin dioxide, which was consistent with the standard data file (JCPDS file no. 41-1445). No other diffraction peaks were observed. In additional, the crystallite size of SnO_2 is about 8.2 nm, which is estimated using the Scherrer formula,

$$D = K\lambda/\beta \cos\theta \quad (3)$$

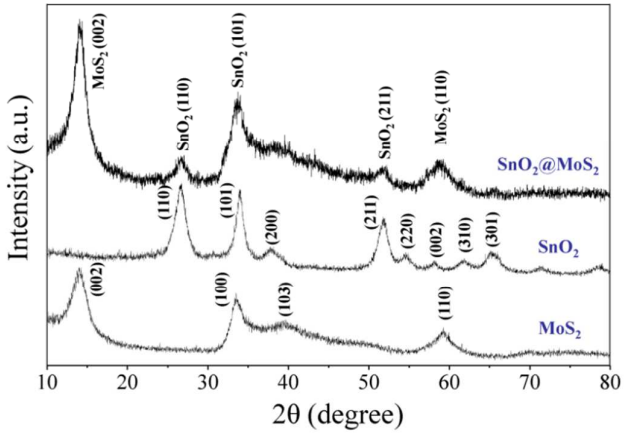

Fig. 1 XRD patterns of pure MoS_2, SnO_2, and SnO_2@MoS_2 composites.

where D is the grain size, K is the Scherrer constant, usually is 0.89, λ is the incident X-ray wavelengths, and β is the wide of the half of the diffraction peak, θ is the Bragg diffraction Angle. The XRD pattern for the SnO_2@MoS_2 composites reveals the presence of individual components of SnO_2 and MoS_2. The diffraction peak at 14.5° is corresponding to the *c*-plane of MoS_2 and can be used to study the structure of MoS_2, which is composed of Mo atoms coordinated with S atoms to form the S-Mo-S sandwich layer.[27] In order to confirm the decoration of Au nanoparticles on the surface of hierarchical MoS_2 nanostructures, XPS analysis was performed and the patterns are presented in Fig. S1. The doublets of Sn $3d_{5/2}$ and $3d_{3/2}$ peaks, located at 487.2 and 494.8 eV, correspond to t the Sn^{4+} of SnO_2.[28] Fig. 3(b) clearly shows the appearance of a spin-orbit doublet at 232.9 ($3d_{3/2}$) and 229.7 eV ($3d_{5/2}$), which is attributed to the Mo^{4+} of MoS_2.[29]

The microstructure and morphology of the as-prepared samples were further characterized by FESEM and TEM. As shown in Fig. 2(a), the surface morphology of pure MoS_2 could be clearly observed from typical FESEM image. It can be seen that hierarchical MoS_2 is flower-like nanosphere with a diameter of about 1.5 μm. A high magnification FESEM image of MoS_2 is shown in Fig. S2(a), indicating large amount of uniform MoS_2 nanosheets. In good agreement with the FESEM image, a low-magnification TEM image (Fig. S2(b)) of a single MoS_2 nanoflower. It can be seen that the flower-like nanostructure is constructed by relatively densely packed nanosheets. Under the examination of TEM (Fig. S1(c)), the MoS_2 nanosheet is fully transparent, showing the extremely small thickness of this 2D structure. With the wrinkles and scrolling, the morphology of the MoS_2 nanosheet is similar to that of a single graphene nanosheet. Moreover, the corresponding SAED pattern (Fig. S1(d)) confirms the hexagonal structure of hierarchical MoS_2 nanostructures and presents well-defined rings that can be well indexed to the XRD patterns. The as-synthesized MoS_2 nanosheets were further decorated with SnO_2 nanoparticles via another hydrothermal process. As shown in Fig. 2(b), SnO_2 nanoparticles dispersed

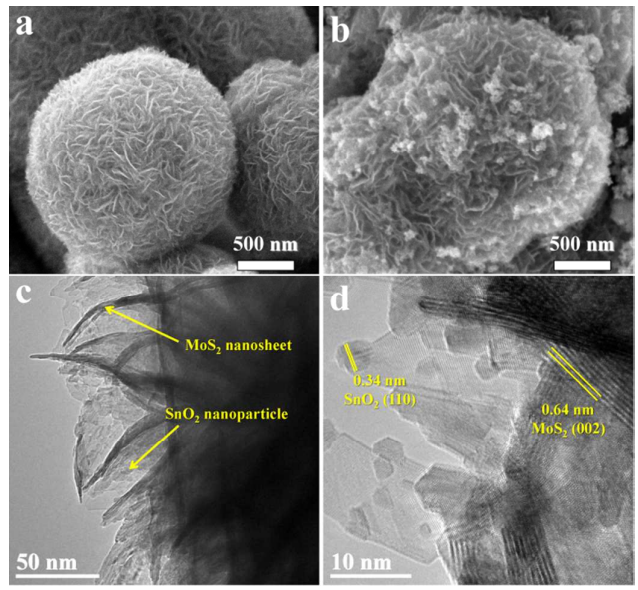

Fig. 2 (a) FESEM image of pure MoS_2, (b) FESEM image and (c and d) TEM images of SnO_2@MoS_2 composites.

on the MoS_2 nanoflower. A few SnO_2 nanoparticles aggregations are observed in FESEM image. The intriguing structure is also elucidated under TEM to provide further insight about the morphology and microstructure. Fig. 2(c) is the TEM image of typical MoS_2 nanosheets inlayed with several dispersive SnO_2 nanoparticles. It can be seen that the sizes of the SnO_2 nanoparticles are less than 10 nm, which is in accord with the results of XRD patterns. Under a higher magnification, the ultrasmall SnO_2 nanoparticles attached on MoS_2 nanosheets can be well observed. The cross-sections of MoS_2 nanosheets can be observed. As shown in Fig. 2(d), the distance between two adjacent atomic planes were calculated to be around 0.64 nm, corresponding to the interplanar distance of (002) plane of hexagonal MoS_2 crystalline structure. The lattices of SnO_2 nanoparticles can be also clearly observed with the interplanar distance of 0.34 nm, matching the (110) plane of cubic SnO_2 crystalline structure (JCPDS 41-1445).

On the basis of the results stated above, the formation process of SnO_2@MoS_2 composites in hydrothermal system is concluded. First, sodium molybdate was chosen as the precursor for molybdenum and thioacetamide was used as the sulfur source. During the hydrothermal treatment, MoO_4^{2-} anions were reduced under high temperature condition, forming MoS_2 nanoparticles.[30,31] Second, these nanoparticles grow up into nanosheet structures in order to reduce the high surface energy through the process known as oriented aggregation. As the reaction further proceeds, the nanosheets tend to merge together to well-defined MoS_2 nanoflowers through a self-assembly process.[32,33] In addition, the formation of SnO_2 nanoparticles adhering on the MoS_2 can be expressed as follows:[34,35]

$$Sn^{4+} + 6OH^- \rightarrow Sn(OH)_6^{2-} \quad (4)$$

$$Sn(OH)_6^{2-} \rightarrow SnO_2 + 2H_2O \quad (5)$$

To explore the advantages of the SnO_2@MoS_2 composites, the as-prepared product was evaluated as sensing material to investigate its gas sensing performance. For comparison, the sensing properties of the pure SnO_2 nanoparticles prepared by hydrothermal method were also studied. It is well known that the gas response of semiconductor gas sensors is greatly influenced by the operating temperature. In order to determine the optimum operating temperatures of sensors based on SnO_2@MoS_2 composites and pure SnO_2 nanoparticles, the response of two sensors to 200 ppm ethanol were tested as a function of operating temperature. As shown in Fig. 3, both sensors exhibit peak-shaped dependence on the operating temperature. It can be clearly observed that the ethanol response first increased with working temperature, and then gradually decreased when the temperature further increases. The relative optimum working temperature can be explained as follows: Normally, the reactivity between the target gas and adsorption oxygen needs certain activation energy, which is provided by increasing reaction temperature. At low working temperature, the adsorbed methanol molecules are not activated enough to overcome the activation energy barrier to react with the adsorption oxygen species, while at high temperatures the gas adsorption is too difficult to be adequately compensated for the increased surface reactivity.[36-38] Moreover, it can be observed that the pure SnO_2 nanoparticles have the maximum gas response at 340 °C, whereas SnO_2@MoS_2 composites have the maximum gas response at 280 °C. Compared with pure SnO_2 nanoparticles, SnO_2@MoS_2 composites exhibit superior gas-sensing performances to ethanol.

The response and recovery time is an important factor to evaluate the gas sensing properties of the sensor. The response time was defined as the time required for the variation in resistance to reach 90% of the equilibrium value after a test gas was injected, and the recovery time as the time necessary for the sensor to return to 10% above the original resistance in air after releasing the test gas. Fig. 4(a) shows the dynamic response transient of the SnO_2@MoS_2 composites gas sensor to

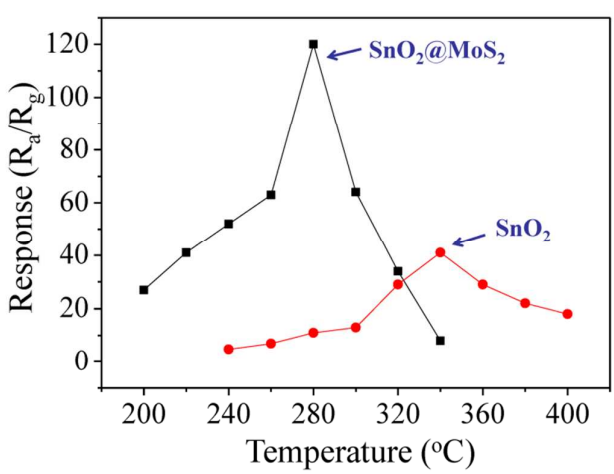

Fig. 3 Correlation between gas response to 200 ppm ethanol and the operating temperature for the sensors based on SnO_2@MoS_2 composites and pure SnO_2 nanoparticles.

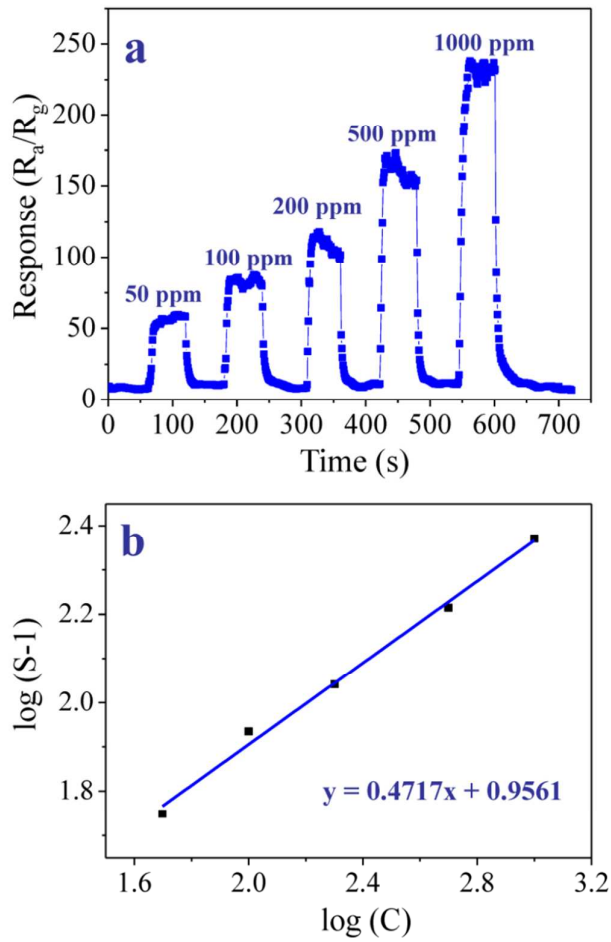

Fig. 4(a) Dynamic response transient of the SnO_2@MoS_2 composites gas sensor to different concentrations of ethanol at 280 °C. (b) Dilogarithm fit curvfe of the response of the sensor to the concentration of ethanol.

different concentrations of ethanol at its optimum operating temperature of 280 °C. It is clear that the response curves of the sensor increases sharply with increasing concentration of ethanol and then returns to the baseline quickly with the ethanol exhausted out in the closed testing chamber, indicating their quick and reversible response and recovery time. Moreover, it can be seen that the response of the sensors increases with the increasing of the ethanol concentrations. The sensor response can be empirically represented as $S = a[C]^b + 1$, where a and b are the constants and S is the gas response, C is the concentration of the test gas.[39,40] Fig. 4(b) shows a chart of logarithm of the response of the sensor (S-1) versus the logarithm of methanol concentration (C). It can be found that the response of the sensor based on SnO_2@MoS_2 composites has a good linear relationship with the ethanol concentration (50-1000 ppm range) in logarithmic forms. As shown in Fig. 3(c), the straight line is the calibration curve ant the experimental data were fitted as: $y = 0.4717*x + 0.9561$, where y is log (S-1) and x is log (C). The results highlighted the potential applications of SnO_2@MoS_2 composites in

monitoring ethanol gas. The selectivity of gas sensors is the ability that a sensor can distinguish different kinds of gases, which is also important for the gas sensing properties. Fig. 5 demonstrated that the gas sensor show responses to various gases of 200 ppm, including ammonia, ethanol, formaldehyde, and acetone. Significantly, the sensor based on SnO_2@MoS_2 composites displayed a much higher response and better selectivity to ethanol as opposed to any other test gases at the working temperature of 280 °C.

SnO_2 is well-known as an n-type gas sensing material and its gas sensing mechanism belongs to the surface-controlled type, the change of resistance is due to the species and the amount of chemisorbed oxygen on the surface. Meanwhile, the tests of gas sensing properties can be explained by the gas sensing mechanism of SnO_2 samples, with the changing in resistance of the sensor upon exposure to different gas atmospheres. When the sensors were exposed to air, the resistance of SnO_2 is controlled by the concentration of adsorbed oxygen species (O_2^-, O^- or O^{2-}) that trap electrons and act as scattering centers effectively reducing the semiconductor conductivity. When the sensor is exposed to ethanol vapor at higher temperature, ethanol reacts with the adsorbed oxygen ions reducing their concentration and thereby increasing the semiconductor conductivity. The possible reactions took place on the surface of tin oxide as follows:[41-43]

$$CH_3CH_2OH + 6O^- \rightarrow 2CO_2 + 3H_2O + 6e^- \quad (6)$$

The SnO_2 sensors change to the initial electronic structure when exposed to air again. The SnO_2@MoS_2 composites exhibit superior gas-sensing performances to ethanol, which is better than that of its counterpart of SnO_2 nanoparticles. That is, there exists a beneficial effect of dispersing SnO_2 nanoparticles on MoS_2 nanosheets. As shown in Fig. 6, the improvement of sensing performance of SnO_2@MoS_2 composites may be attributed to the following reasons. Firstly, MoS_2 nanosheet with high surface area provides a platform for attaching the SnO_2 nanoparticles, preventing their interparticle aggregation. This kind of nanostructure can provide a large specific surface area, which is of great benefit to numerous oxygen molecules adsorbed onto SnO_2 nanoparticles, and facilitate the diffusion

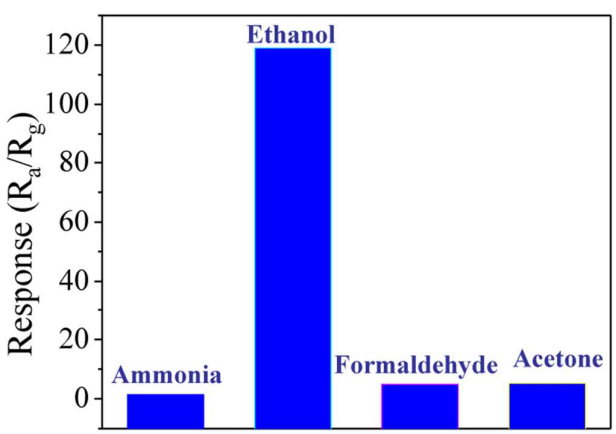

Fig.5 Response fo the sensor based on SnO_2@MoS_2 composites to various test gases.

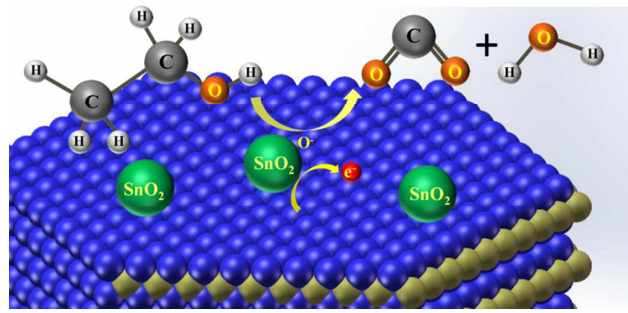

Fig. 6 Schematic of gas-sensing mechanism of an MoS_2 nanosheet decorated with SnO_2 nanoparticles.

of ethanol gas, improving the reaction of the ethanol gas with surface adsorbed oxygen.[44,45] Besides, the operating temperature of SnO_2@MoS_2 composite sensor has a significant decrease, compared to the pure SnO_2 nanoparticles, indicating the surface reaction occurred at a lower operating temperature, which can be attributed to that the activation energy of the surface reaction is lowered by mixing MoS_2 nanosheets. In this work, MoS_2 nanosheet with high surface area provides a platform for attaching the SnO_2 nanoparticles, preventing their interparticle aggregation. The crystallite size of SnO_2 is less than 10 nm, which is estimated by XRD patterns and TEM image. Under this conditions, very low activation energy for the grain growth has been calculated for SnO_2 nanocrystallites within the size range of 3–20 nm. While, above this size range (20–300 nm), the activation energy for the grain growth increases exponentially.[46,47] Secondly, the significant increase of the gas-sensing performance for SnO_2@MoS_2 composites can be attributed to the active site provided by the MoS_2 nanosheets and also the good interaction between the two materials,[48] therefore improving the electron transfer rate, and thus enhancing gas-sensing response. Thirdly, the MoS_2 nanosheet in this work exhibits a p-type semiconducting behavior in air, which is similar to literatures.[49-53] Thus, at the interface between the SnO_2 nanoparticles and the MoS_2 nanosheets, there forms a p-n junction, which will result in the MoS_2 and SnO_2 having a same Fermi energy level at the interface. Thus a staggered band offset and a built-in internal electric field was formed near the interface. When SnO_2@MoS_2 composites are exposed to ethanol vapor at higher temperature, electrons generate in the reaction can easily cross the interface and transfer to the conductive band of SnO_2 nanoparticles Because the conduction band and the valence band of SnO_2 both lie below the energy band of MoS_2 in this composite. As a result, the gas-sensing performance can thus be improved eventually in the composites of dispersing SnO_2 nanoparticles on the surfaces of MoS_2 nanosheets. Furthermore, to reveal the influence of the content of SnO_2 in composites, the study of morphology and gas response of SnO_2@MoS_2 composites with different reaction conditions was investigated by changing the MoS_2/SnO_2 molar ratios, while temperature and reaction time were kept at 200 °C and 21 h, respectively (Fig. S3).

Conclusions

In summary, a simple solution route was successfully promoted to synthesize novel gas-sensing composite by dispersing SnO_2 nanoparticles on the surfaces of MoS_2 nanosheets. Importantly, it is found that MoS_2 nanosheets play an important role for enhancing the gas-sensing performance. The SnO_2@MoS_2 composite sensor exhibits better gas-sensing performance in comparison with pure SnO_2 nanoparticles, indicating the potential applications as gas sensor material toward ethanol detection.

Acknowledgements

This work was financially supported by National Natural Science Foundation of China (No. 61102006 and 51172095), Natural Science Foundation of Shandong Province, China (No. ZR2015EM019 and ZR2014EL006), and Shandong Province Higher Educational Science and Technology Program (No. J15LA56).

Notes and references

1 E. Comini, *Anal. Chim. Acta*, 2006, **568**, 28.
2 C. Ucurum and H. Goebel, *Microelectron. J.*, 2013, **44**, 604.
3 A. Tricoli, M. Righettoni and A. Teleki, *Angew. Chem. Int. Edit.*, 2010, **49**, 7632.
4 J. Q. Xu, D. Wang, L.P. Qin, W.J. Yu and Q.Y. Pan, *Sensor. Actuat. B*, 2009, **137**, 490.
5 L.L. Wang, T. Fei, Z. Lou and T. Zhang, *ACS Appl. Mater. Interfaces*, 2011, **3**, 4689.
6 Z.D. Lin, F. Guo, C. Wang, X.H. Wang, K. Wang and Y. Qu, *RSC Adv*, 2014, **4**, 5122.
7 H.K. Wang and A. L. Rogach, *Chem. Mater.*, 2014, **26**, 123.
8 E.R. Leite, I.T. Weber, E. Longo and J.A. Varela, *Adv. Mater.*, 2000, **12**, 965.
9 L.P. Qin, J.Q. Xu, X.W. Dong, Q.Y. Pan, Z.X. Cheng, Q. Xiang and F. Li, *Nanotechnology*, 2008, **19**, 185705.
10 J.R. Huang, K. Yu, C.P. Gu, M.H. Zhai, Y.J. Wu, M. Yang and J.H. Liu, *Sens. Actuators B*, 2010, **147**, 467.
11 Y. Guan, D.W. Wang, X. Zhou, P. Sun, H.Y. Wang, J. Ma and G.Y. Lu, *Sens. Actuators B*, 2014, **191**, 45.
12 C.J. Huang, W.Q. Ye, Q.W. Liu and X.Q. Qiu, *ACS Appl. Mater. Interfaces*, 2014, **6**, 14469.
13 H. Fei, Z. Peng, L. Li, Y. Yang, W. Lu, E.L. Samuel, X. Fan and J.M. Tour, *Nano Res.*, 2014, **7**, 1.
14 D. Wang, D. Choi, J. Li, Z. Yang, Z. Nie, R. Kou, D. Hu, C. Wang, L.V. Saraf and J. Zhang, *ACS Nano*, 2009, **3**, 907.
15 G. Wang, X. Tan, Q. Zhou, Y. Liu, M. Wang and L. Yang, *Sens. Actuators B*, 2014, **190**, 730.
16 W. Li, F. Wang, S. Feng, J. Wang, Z. Sun, B. Li, Y. Li, J. Yang, A.A. Elzatahry and Y. Xia, *J. Am. Chem. Soc.*, 2013, **135**, 18300.
17 H. Wang, H.B. Feng and J.H. Li, *Small*, 2014, **10**, 2165.
18 G. Neri, S.G. Leonardi, M. Latino, N. Donato, S. Baek, D.E. Conte, P.A. Russo and N. Pinna, *Sens. Actuators B*, 2013, **179**, 61.
19 S.M Liang, J.W. Zhu, C. Wang, S.T. Yu, H.P. Bi, X.H. Liu and X. Wang, *Appl. Surf. Sci.*, 2014, **292**, 278.
20 R.F. Service, *Science*, 2015, **348**, 490.
21 M.S. Xu, T. Liang, M.M. Shi and H.Z. Chen, *Chem. Rev.*, 2013, **113**, 3766.
22 C.N.R.Rao, H.S.S.R. Matte and U. Maitra, *Angew. Chem. Int. Ed.*, 2013, **52**, 13162.
23 K.P. Wang, J. Wang, J.T. Fan, M. Lotya, A. O'Neill, D. Fox, Y.Y. Feng, X.Y. Zhang, B.X. Jiang, Q.Z. Zhao, H.Z. Zhang, J.N. Coleman, L. Zhang and W.J. Blau, *ACS Nano*, 2013, **7,** 9260.
24 H. Li, Z.Y. Yin, Q.Y. He, H. Li, X. Huang, G. Lu, D.W.H. Fam, A.Y. Tok, Q. Zhang and H. Zhang, *Small*, 2012, **8**, 63.
25 D.J. Late, Y.K. Huang, B. Liu, J. Acharya, S.N. Shirodkar, J.Y. Luo, A.M. Yan, D. Charles, U.V. Waghmare, V.P. Dravid and C.N.R. Rao, *ACS Nano*, 2013, **7**, 4879.
26 F.K. Perkins, A.L. Friedman, E. Cobas, P.M. Campbell, G.G. Jernigan and B.T. Jonker, *Nano Lett.*, 2013, **13**, 668.
27 W.J. Zhou, Z.Y. Yin, Y.P. Du, X. Huang, Z.Y. Zeng, Z.X. Fan, H. Liu, J.Y. Wang and H. Zhang, *Small*, 2013, **9**, 140.
28 V.V. Sysoev, J. Goschnick, T. Schneider, E. Strelcov and A. Kolmakov, *Nano Lett.*, 2007, **7**, 3182.
29 Y. Liu, Y.X. Yu and W.D. Zhang, *J. Phys. Chem. C*, 2013, **117**, 12949.
30 26 Y.D. Li, X.L. Li, R.R. He, J. Zhu, Z.X. Deng, *J. Am. Chem. Soc.*, 2002, **124**, 1411.
31 27 C. Pacholski, A. Kornowski, H. Weller, *Angew. Chen. –Int Edit*, 2002, **41**, 1188.
32 28 G.G. Tang, J.R. Sun, C. Wei, et al. *Mater. Lett.*, 2012, **86**, 9.
33 29 Y. Cheng, Y.S. Wang, Y.H. Zheng, Y. Qin, J. *Phys. Chem. B*, 2005, **109**, 11548.
34 M.T. Niu, F. Huang, L.F. Cui, P. Huang, Y.L. Yu and Y.S. Wang, ACS Nano, 2010, 4, 681.
35 O. Lupan, L. Chow, G. Chai, A. Schulte, S. Park and H. Heinrich, Mater. Sci. Eng. B, 2009, 157, 101.
36 Z. Lou, J. N. Deng, L. L. Wang, L. J. Wang, T. Fei and T. Zhang, *Sens. Actuators B*, 2013, **176**, 323.
37 L.J. Bie, X.N. Yan, J. Yin, Y.Q. Duan and Z.H. Yuan, *Sens. Actuators B*, 2007, **126**, 604.
38 P. Sun, X. Zhou, C. Wang, K. Shimanoe, G. Lu and N Yamazoe, *J. Mater. Chem. A.*, 2014, **2**, 1302.
39 N. Yamazoe, K. Shimanoe, *Sens. Actuators B*, 2008, **128**, 566.
40 X.J. Liu, Z. Chang, L. Luo, X.D. Lei, J.F. Liu, X.M. Sun, *J. Mater. Chem.*, 2012, **22**, 7232.
41 J.Q. Xu, J.J. Han, Y. Zhang, Y.A. Sun and B. Xie, *Sens. Actuators B*, 2008, **132**, 334.
42 H. Men, P. Gao, B.B. Zhou, Y.J. Chen, C.L. Zhu, G. Xiao, L.Q. Wang and M.L. Zhang, *Chem. Commun.*, 2010, **46**, 7581.
43 L.Q. Wang, P. Gao, D. Bao, Y. Wang, Y.J. Chen, C. Chang, G.B. Li and P.P. Yang, *Cryst. Growth Des.*, 2014, **14**, 569.
44 M. Zhou, Y. Lu, Y. Cai, C. Zhang and Y. Feng, *Nanotechnology*, 2011, **22**, 385502.
45 R.K. Joshi, H. Gomez, F. Alvi and A. Kumar, *J. Phys. Chem. C*, 2010, **114**, 6610.
46 S. Shukla and S. Seal, *J. Nanosci. Nanotechnol.*, 2004, **4**, 141.
47 S. Shukla, S. Seal, L. Ludwig and C. Parish, *Sens. Actuators B*, 2004, **97**, 256.

48 Y.F. Zhao, Z.Y. Yang, Y.X. Zhang, L. Jing, X. Guo, Z.T. Ke, P.W. Hu, G.X. Wang, Y.M. Yan and K.N. Sun, *J. Phys. Chem. C*, 2014, **118**, 14238.
49 J. Wu, H. Li, Z.Y. Yin, H. Li, J.Q. Liu, X.H. Cao, Q. Zhang and H. Zhang, *Small*, 2013, **9**, 3314.
50 Y. Liu, Y.X. Yu and W.D. Zhang, *J. Phys. Chem. C*, 2013, **117**, 12949.
51 J. Heising and M.G. Kanatzidis, *J. Am. Chem. Soc.*, 1999, **121**, 11720.
52 E. Gourmelon, J.C. Bernede, J. Pouzet and S. Marsillac, *J. Appl. Phys.*, 2000, **87**, 1182.
53 J.G. He, K.C. Wu, R.J. Sa, Q.H. Li and Y.Q. Wei, *Appl. Phys. Lett.*, 2010, **96**, 082504.